SAND2015-1656J

A Modified Stillinger-Weber Potential for TlBr, and Its Polymorphic Extension

X. W. Zhou[1], M. E. Foster[2], Reese Jones[1], and F. P. Doty[3], P. Yang[4], and H. Fan[5,6]

[1]*Mechanics of Materials Department, Sandia National Laboratories, Livermore, California 94550, USA, Email: xzhou@sandia.gov*

[2]*Materials Chemistry Department, Sandia National Laboratories, Livermore, California 94550, USA*

[3]*Radiation and Nuclear Detection Materials and Analysis Department, Sandia National Laboratories, Livermore, California 94550, USA*

[4]*Electronic, Optical, and Nano Department, Sandia National Laboratories, Albuquerque, NM 87106, USA*

[5]*Advanced Materials Laboratory, Sandia National Laboratories, Albuquerque, NM 87106, USA*

[6]*Center for Micro-Engineered Materials, Department of Chemical and Biological Engineering, University of New Mexico, Albuquerque, NM 87106, USA*

ABSTRACT

TlBr has emerged to be one of the most promising materials for γ- and x- radiation detection in recent years. Unfortunately, the performance of this material degrades rapidly due to the structural changes caused by ionic conduction. To enable molecular dynamics simulations of structure evolution of TlBr under external electric fields, we have developed a Stillinger-Weber type of TlBr interatomic potential. During this process, we also have addressed two problems of wider interests. First, while being simple and suitable for a rapid development, the conventional

Stillinger-Weber potential format is only applicable for tetrahedral structures (e.g., diamond-cubic, zinc-blende, or wurtzite). Here we have modified the analytical functions of the Stillinger-Weber potential so that it can now be used for other crystal structures. Second, past improvement of interatomic potentials cannot always be applied by a broad community because any modifications of the analytical functions of the potential would require corresponding changes in the molecular dynamics codes. Here we have developed a polymorphic potential model, and implemented it as a new pair style in the public molecular dynamics codes LAMMPS. This pair style takes tabular (rather than analytical) potential functions. Depending on the tables that users supplied, our polymorphic potential reduces automatically to Stillinger-Weber, Tersoff, embedded-atom method, and any variations (i.e., modified functions) of these potentials. Simulations using the polymorphic model are carried out to evaluate the fidelity of our TlBr potential. In particular, challenging simulations of ionic conduction under external electric fields are demonstrated.

Keywords: interatomic potential, molecular dynamics, TlBr crystal.

1. INTRODUCTION

Thallium bromide (TlBr) has emerged to be one of the most promising materials for γ- and x- radiation detection in recent years, achieving resolution as high as 1% at 662 keV [1,2]. Unfortunately, the performance of this material degrades after operation times as short as a few hours to a few weeks [3]. To extend the life time of TlBr crystals, the evolution of the atomic scale structures of the materials due to ionic conduction under the operating external electric fields must be understood. As ionic conduction may be facilitated by the open channels of edge dislocations, molecular dynamics (MD) that allows extended defects to be included in simulated

crystals becomes a useful method to study structure evolution of TlBr. Such MD simulations are not yet possible due to the lack of an interatomic potential for the Tl-Br system that has a CsCl type of crystal structure.

MD simulations of ionic diffusion have been applied to a number of compounds including CuI [4,5], M3+ doped CeO_2 [6], zirconia [7,8,9], α-LiI [10], alumina [10,11], and CaF_2 [12]. These simulations do not apply external electric fields, and therefore the ionic conduction is indirectly deduced from thermal diffusion. Our objective is to simulate directly the ionic conduction under external electric fields. One advantage is that the ionic diffusion can be accelerated by the external fields, therefore mitigating the short time scale issue of MD simulations. This, however, imposes a more stringent requirement on the interatomic potential for maintaining the crystal even when a large external field is applied (i.e., cations and anions are subject to large opposite forces). The previous simulations use either pair potentials [5-9,12], or pair potentials plus angular energy penalty interactions [10,11]. The angular energy penalty interactions can stabilize relatively complex crystal structures that the pair potentials cannot. One good example is the widely-used Stillinger-Weber (SW) potential [13], which uses a parabolic energy penalty term to penalize non-tetrahedral bond angles. As a result, SW potentials have been successfully applied to tetrahedral structures such as diamond-cubic, zinc-blende, and wurtzite[*]. Depending on parameterization, SW potentials can also be used for fcc elements [14,15,16]. However, the conventional SW potentials have two limitations [14,15,16]: (1) they significantly overestimate the elastic constants of closely packed (e.g., fcc) elements; and (2) they usually cannot be used for other (non-tetrahedral) structures such as sc elements, and NaCl and CsCl compounds. Note that although most elements do not exhibit the lowest energy for the

[*] For convenience, we will use abbreviation to represent structures in the following: dc: diamond-cubic; sc: simple-cubic; bcc: body-centered-cubic; fcc: face-centered-cubic; hcp: hexagonal-closely-packed; zb: zinc-blende; wz: wurtzite; NaCl: B1; and CsCl: B2.

sc crystal structure, the sc crystal can have a near-lowest energy that cannot be captured by SW potentials. Potentials capable of prescribing a low energy for the sc structure, therefore, improve beyond SW potentials on the general energy trends when a variety of configurations are considered [17].

Many literature potentials are constructed using particular analytical functions. These potentials can be easily improved if alternative functions are used. For example, Rockett [18] used alternative functions for the Tersoff [19,20] potentials to better treat short- and long- range interactions in covalent systems, and we used alternative functions for the Tersoff potential to improve its prediction on thermal conductivity [21]. Although alternative functions do not change the potential format and should, therefore, be easily applied, such an approach has not been widely used because it does require new molecular dynamics codes to be developed for each modified function.

With the recognition that the problems described above have been limiting the atomistic level studies of emerging important materials, the objective of the present work is threefold: (1) modify the SW potential so that it can better describe elastic constants of elements and be applicable to a wide range of crystal structures including sc, NaCl, and CsCl; (2) develop a polymorphic potential model that incorporates simultaneously SW potential, modified SW potential, Tersoff potential [19,20], modified Tersoff potential [18], and embedded-atom method (EAM) potential [22]. Implement this polymorphic potential model in public MD codes LAMMPS [23] so that future development of potentials using any alternative functions no longer requires modification of the molecular dynamics codes; and (3) parameterize the modified SW potential for TlBr system and demonstrate the utility of the resulting potential.

2. MODIFIED SW POTENTIALS

In SW potential [13], the total energy of a system of N atoms is expressed as

$$E = \frac{1}{2}\sum_{i=1}^{N}\sum_{j=i_1}^{i_N}\left[\phi_{R,IJ}(r_{ij}) - \phi_{A,IJ}(r_{ij}) + u_{IJ}(r_{ij})\sum_{\substack{k=i_1 \\ k\neq j}}^{i_N} u_{IK}(r_{ik})\cdot g_{JIK}(\cos\theta_{jik})^2\right] \quad (1)$$

where i_1, i_2, …, i_N is a list of neighbors of atom i, θ_{jik} is the bond angle formed by atoms j and k at the site of atom i, $\phi_{R,IJ}(r_{ij})$ and $\phi_{A,IJ}(r_{ij})$ are, respectively, pairwise repulsive and attractive functions, $u_{IJ}(r_{ij})$ is another pair function, $g_{JIK}(\cos\theta_{jik})$ is an angular energy penalty function, and subscripts i,j,k and I,J,K indicate, respectively, the atoms and the species of the atoms (note that three bodies JIK and KIJ are equivalent). The original SW potentials significantly overestimate the elastic constants of elements because the $\phi_{R,IJ}(r)$ and $\phi_{A,IJ}(r)$ functions used in these potentials do not allow independent adjustment of bond energy and second derivative of the bond energy [14]. Here we propose to use Morse type of functions capable of independent change of bond energy and second derivative of bond energy [14] to represent $\phi_{R,IJ}(r)$ and $\phi_{A,IJ}(r)$:

$$\phi_{R,IJ}(r) = \frac{E_{b,IJ}\cdot\beta_{IJ}}{\beta_{IJ}-\alpha_{IJ}}\cdot\exp\left(-\alpha_{IJ}\cdot\frac{r-r_{0,IJ}}{r_{0,IJ}}\right)\cdot f_{c,IJ}(r), \quad (2)$$

$$\phi_{A,IJ}(r) = \frac{E_{b,IJ}\cdot\alpha_{IJ}}{\beta_{IJ}-\alpha_{IJ}}\cdot\exp\left(-\beta_{IJ}\cdot\frac{r-r_{0,IJ}}{r_{0,IJ}}\right)\cdot f_{c,IJ}(r), \quad (3)$$

where $E_{b,IJ}$, $r_{0,IJ}$, α_{IJ}, and β_{IJ} are four pair dependent parameters, and $f_{c,IJ}(r_{ij})$ is a cutoff function. Note that the parameters introduced here have physical meanings: $E_{b,IJ}$ and $r_{0,IJ}$ correspond respectively to the equilibrium bond energy and bond length, and $\alpha_{IJ} >> \beta_{IJ}$ control the curvature of the bond energy at the equilibrium bond length. The cutoff function $f_{c,IJ}(r_{ij})$ is expressed as:

$$f_{c,IJ}(r) = \begin{cases} \dfrac{\exp\left(-\varsigma_{IJ}\cdot r^{\upsilon_{IJ}}\right) - \exp\left(-\varsigma_{IJ}\cdot r_{c,IJ}^{\upsilon_{IJ}}\right)}{\exp\left(-\varsigma_{IJ}\cdot r_{s,IJ}^{\upsilon_{IJ}}\right) - \exp\left(-\varsigma_{IJ}\cdot r_{c,IJ}^{\upsilon_{IJ}}\right)}, & r \le r_{c,IJ} \\ 0, & r > r_{c,IJ} \end{cases} \quad (4)$$

where $r_{s,IJ}$ and $r_{c,IJ}$ ($r_{s,IJ} << r_{c,IJ}$) are two independent pair parameters, and ζ_{IJ} and υ_{IJ} are two dependent pair parameters $\upsilon_{IJ} = \frac{\ln[\ln(0.9)/\ln(0.00000001)]}{\ln(r_{s,IJ}/r_{c,IJ})}$ and $\varsigma_{IJ} = -\frac{\ln(0.9)}{(r_{s,IJ})^{\upsilon_{IJ}}}$. Note that $r_{s,IJ}$ and $r_{c,IJ}$ have physical meanings as the cutoff function approximately equals one at $r \le r_{s,IJ}$ and equals zero at $r = r_{c,IJ}$ (i.e., $r_{c,IJ}$ is the cutoff distance). Hence, multiplying any potential function with this cutoff function does not affect significantly the potential function at small distances but allows the potential function to be smoothly cut off at $r_{c,IJ}$. Such a cutoff method is superior to the spline approach used by the Tersoff potential as the latter does not have continuous second and higher order derivatives. A general exponential decay function is used to represent the $u_{IJ}(r)$ function:

$$u_{IJ}(r) = \exp\left(-\gamma_{IJ} \cdot \frac{r_{ij} - r_{0,IJ}}{r_{0,IJ}}\right) \cdot f_{c,IJ}(r_{ij}) \tag{5}$$

where γ_{IJ} is a pair parameter.

For the angular function, SW potentials use a parabolic energy penalty to the non-tetrahedral angle $g_{JIK}(\cos\theta_{jik}) = (\cos\theta_{jik}-\cos\theta_{0,JIK})^2$ where the parameter $\cos\theta_{0,JIK}$ is fixed at the tetrahedral bond angle $\cos\theta_{0,JIK} = -1/3$. This function can be made more general by treating $\cos\theta_{0,JIK}$ as a fitting parameter. Even so, the resulting function is still not fully flexible, for instance, it does not have a scaling factor, and its second derivative is fixed at 2. In addition, the function is symmetric at $\cos\theta_{jik} = \cos\theta_{0,JIK}$, and the energy penalty does not saturate (i.e., the absolute slope increases when the angle deviates from $\cos\theta_{0,JIK}$). These cause difficulties for capturing the angular function derived from quantum mechanical theories [24]. Here we consider a new angular function $g_{JIK}(\cos\theta_{jik}) = \lambda_{JIK}\cdot\{1-\exp[-\xi_{0,JIK}\cdot(\cos\theta_{jik}-\cos\theta_{0,JIK})^2]\}$, where λ_{JIK} is three-body dependent scaling factor and $\xi_{0,JIK}$ is another three-body dependent parameter. Note

that for $\lambda_{JIK} = 1$, $\xi_{0,JIK} = 1$ and $\cos\theta_{0,JIK} = -1/3$, the modified energy penalty is equivalent to the parabolic function near $\cos\theta_{jik} = -1/3$ because the first term of the Taylor series of the modified function expanded at $\cos\theta_{jik} = \cos\theta_{0,JIK}$ is in fact the parabolic function. However, replacing the leading term with a full series does allow the energy penalty curvature to be adjusted through an added parameter $\xi_{0,JIK}$ and the value of function to be saturated (while retaining the "penalty" effect, i.e., the function minimizes at $\cos\theta_{jik} = \cos\theta_{0,JIK}$ and monotonically increases when $\cos\theta_{jik}$ deviates from $\cos\theta_{0,JIK}$). An even further flexible function will be to penalize the energy when the bond angle deviates from three independent values, which also results in asymmetric minimums. Based on this consideration, we propose a general angular function as:

$$g_{JIK}(\cos\theta_{jik}) = \lambda_{JIK} \cdot \frac{1-\exp\left[-\xi_{0,JIK}\cdot\left(\cos\theta_{jik}-\cos\theta_{0,JIK}\right)^2\right]}{1-\exp\left[-\xi_{0,JIK}\cdot\left(1-\cos\theta_{0,JIK}\right)^2\right]}\cdot \frac{1-\kappa_{1,JIK}\cdot\exp\left[-\xi_{1,JIK}\cdot\left(\cos\theta_{jik}-\cos\theta_{1,JIK}\right)^2\right]}{1-\kappa_{1,JIK}\cdot\exp\left[-\xi_{1,JIK}\cdot\left(1-\cos\theta_{1,JIK}\right)^2\right]}\cdot \frac{1-\kappa_{2,JIK}\cdot\exp\left[-\xi_{2,JIK}\cdot\left(\cos\theta_{jik}-\cos\theta_{2,JIK}\right)^2\right]}{1-\kappa_{2,JIK}\cdot\exp\left[-\xi_{2,JIK}\cdot\left(1-\cos\theta_{2,JIK}\right)^2\right]} \quad (6)$$

where λ_{JIK}, $\xi_{0,JIK}$, $\xi_{1,JIK}$, $\xi_{2,JIK}$, $\cos\theta_{0,JIK}$, $\cos\theta_{1,JIK}$, $\cos\theta_{2,JIK}$, $\kappa_{1,JIK}$, and $\kappa_{2,JIK}$ are all three-body dependent parameters. Note that when the parameters are given, the denominator in Eq. (6) is essentially a normalization constant so that $g_{JIK}(\cos\theta_{jik}=1) = \lambda_{JIK}$. It can be seen that when $\kappa_{1,JIK} = \kappa_{2,JIK} = 0$, Eq. (6) penalizes the energy when the bond angle deviates from a single value $\cos\theta_{jik} = \cos\theta_{0,JIK}$ as in the conventional SW potential. Otherwise Eq. (6) can penalize the energy when the bond angle deviates from three values $\cos\theta_{jik} = \cos\theta_{0,JIK}$, $\cos\theta_{jik} = \cos\theta_{1,JIK}$, $\cos\theta_{jik} = \cos\theta_{2,JIK}$. Eqs. (1) – (6) fully define our modified SW (MSW) potential.

3. POLYMORPHIC POTENTIAL MODEL

Any improved interatomic potentials will not be applied unless molecular dynamics codes are available to run them. To provide potential developers with a great flexibility for modifying

the interatomic potentials without worrying about MD codes, we have constructed a polymorphic potential model. In this model, the energy of the system is expressed as

$$E = \frac{1}{2}\sum_{i=1}^{N}\sum_{j=1}^{N}\left[\left(1-\delta_{ij}\right)\cdot U_{IJ}\left(r_{ij}\right)-\left(1-\eta_{ij}\right)\cdot F_{IJ}\left(\mathrm{X}_{ij}\right)\cdot V_{IJ}\left(r_{ij}\right)\right] \tag{7}$$

where δ_{ij} is a Dirac function (i.e., $\delta_{ij} = 1$ when i = j and $\delta_{ij} = 0$ when $i \neq j$), η_{ij} is an indicator of the potential type that can be set to either $\eta_{ij} = \delta_{ij}$ or $\eta_{ij} = 1- \delta_{ij}$, $U_{IJ}(r_{ij})$ and $V_{IJ}(r_{ij})$ are two pair functions, and $F_{IJ}(X_{ij})$ is a function of a local variable X_{ij} that will be discussed below. It can be seen that when $\eta_{ij} = \delta_{ij}$, the summation in equation (7) excludes the self-interaction term i = j and is therefore over all pairs of different atoms. When $\eta_{ij} = 1 - \delta_{ij}$, the second term becomes $E = \frac{1}{2}\sum_{i=1}^{N} F_{II}\left(\mathrm{X}_{ii}\right)\cdot V_{II}\left(r_{ii}\right)$, which can be used to incorporate the embedding energy of the embedded-atom method as will be clear later in this section. The variable X_{ij} essentially accounts for the environment surrounding the ij bond, and is defined as

$$X_{ij} = \sum_{\substack{k=i_1 \\ k\neq i,j}}^{i_N} W_{IK}\left(r_{ik}\right)\cdot G_{JIK}\left(\theta_{jik}\right)\cdot P_{IK}\left(\Delta r_{jik}\right)\cdot \tag{8}$$

where $P_{IJ}(\Delta r_{jik})$ is a function of weighted difference between atomic spacing r_{ij} and r_{ik}, which is written as $\Delta r_{jik} = r_{ij} - \xi_{IJ}\cdot r_{ik}$ with the weighting factor ξ_{IJ} being either 0 or 1 to include or exclude r_{ik}, $W_{IK}(r_{ik})$ is another pair function, and $G_{JIK}(\theta_{jik})$ is a three-body function of bond angle θ_{jik}. It can be seen that this polymorphic interatomic potential model is fully defined when the indicators η_{ij} and ξ_{IJ}, and the six functions $U_{IJ}(r)$, $V_{IJ}(r)$, $P_{IJ}(\Delta r)$, $W_{IJ}(r)$, $F_{IJ}(X)$, and $G_{JIK}(\theta)$ (for all the species I, J, K = 1, 2, …) are given. Note that these six functions can all be supplied as one-dimensional tables and can therefore be implemented in MD codes using cubic spline interpolation and/or extrapolation. As a result, users can easily perform simulations using

different potentials by tabulating these functions (in a MD read-in table file) accordingly. For instance, the polymorphic potential reduces to our MSW potential if we tabulate the functions according to:

$$\begin{cases} \eta_{ij} = \delta_{ij}, \xi_{IJ} = 0 \\ U_{IJ}(r) = \phi_{R,IJ}(r) - \phi_{A,IJ}(r) \\ V_{IJ}(r) = u_{IJ}(r) \\ F_{IJ}(X) = -X \\ P_{IJ}(\Delta r) = 1 \\ W_{IJ}(r) = u_{IJ}(r) \\ G_{JIK}(\theta) = g_{JIK}(\theta) \end{cases} \tag{9}$$

where $\phi_{R,IJ}(r)$, $\phi_{A,IJ}(r)$, $u_{IJ}(r)$, and $g_{JIK}(\cos\theta)$ are defined by Eqs. (2), (3), (5) and (6). The polymorphic potential reduces to a conventional SW [13] potential if we tabulate the functions according to:

$$\begin{cases} \eta_{ij} = \delta_{ij}, \xi_{IJ} = 0 \\ U_{IJ}(r) = A_{IJ} \cdot \varepsilon_{IJ} \cdot \left(\frac{\sigma_{IJ}}{r}\right)^q \cdot \left[B_{IJ}\left(\frac{\sigma_{IJ}}{r}\right)^{p-q} - 1\right] \cdot \exp\left(\frac{\sigma_{IJ}}{r - a_{IJ} \cdot \sigma_{IJ}}\right) \\ V_{IJ}(r) = \sqrt{\lambda_{IJ} \cdot \varepsilon_{IJ}} \cdot \exp\left(\frac{\gamma_{IJ} \cdot \sigma_{IJ}}{r - a_{IJ} \cdot \sigma_{IJ}}\right) \\ F_{IJ}(X) = -X \\ P_{IJ}(\Delta r) = 1 \\ W_{IJ}(r) = \sqrt{\lambda_{IJ} \cdot \varepsilon_{IJ}} \cdot \exp\left(\frac{\gamma_{IJ} \cdot \sigma_{IJ}}{r - a_{IJ} \cdot \sigma_{IJ}}\right) \\ G_{JIK}(\theta) = \left(\cos\theta + \frac{1}{3}\right)^2 \end{cases} \tag{10}$$

where A_{IJ}, B_{IJ}, ε_{IJ}, σ_{IJ}, λ_{IJ}, γ_{IJ}, a_{IJ}, p, and q are the normal parameters for the SW potential as described above. The polymorphic model represents Tersoff types of potential [19,20] if we set

$$\begin{cases} \eta_{ij} = \delta_{ij}, \xi_{IJ} = 1 \\ U_{IJ}(r) = \dfrac{D_{e,IJ}}{S_{IJ} - 1} \exp\left[-\beta_{IJ} \sqrt{2S_{IJ}} \left(r - r_{e,IJ} \right) \right] \cdot f_{c,IJ}(r) \\ V_{IJ}(r) = \dfrac{S_{IJ} \cdot D_{e,IJ}}{S_{IJ} - 1} \exp\left[-\beta_{IJ} \sqrt{\dfrac{2}{S_{IJ}}} \left(r - r_{e,IJ} \right) \right] \cdot f_{c,IJ}(r) \\ F_{IJ}(X) = (1 + X)^{-\frac{1}{2}} \\ P_{IK}(\Delta r) = \exp\left[2\mu_{IK} \cdot \Delta r \right] \\ W_{IK}(r) = f_{c,IK}(r) \\ G_{JIK}(\theta) = \gamma_{IK} \left[1 + \dfrac{c_{IK}^2}{d_{IK}^2} - \dfrac{c_{IK}^2}{d_{IK}^2 + (h_{IK} + \cos\theta)^2} \right] \end{cases} \tag{11}$$

where $f_{c,IJ}(r_{ij})$ is a cutoff function defined as

$$f_{c,IJ}(r) = \begin{cases} 1, & r \le r_{s,IJ} \\ \dfrac{1}{2} + \dfrac{1}{2} \cos\left[\dfrac{\pi (r - r_{s,IJ})}{r_{c,IJ} - r_{s,IJ}} \right], & r_{s,IJ} < r < r_{c,IJ} \\ 0, & r \ge r_{c,IJ} \end{cases} \tag{12}$$

and $D_{e,IJ}$, S_{IJ}, $r_{e,IJ}$, β_{IJ}, μ_{IJ}, γ_{IJ}, c_{IJ}, d_{IJ}, h_{IJ}, $r_{s,IJ}$ and $r_{c,IJ}$ are all pairwise parameters. The polymorphic potential can also represent the Rockett-Tersoff potential [18] if we set

$$\begin{cases} \eta_{ij} = \delta_{ij}, \xi_{IJ} = 1 \\ U_{IJ}(r) = \begin{cases} A_{IJ} \cdot \exp\left(-\lambda_{1,IJ} \cdot r \right) \cdot f_{c,IJ}(r), & r \le r_{s,1,IJ} \\ A_{IJ} \cdot \exp\left(-\lambda_{1,IJ} \cdot r \right) \cdot f_{c,IJ}(r) \cdot f_{c,1,IJ}(r), & r_{s,1,IJ} < r < r_{c,1,IJ} \\ 0, & r \ge r_{c,1,IJ} \end{cases} \\ V_{IJ}(r) = \begin{cases} B_{IJ} \cdot \exp\left(-\lambda_{2,IJ} \cdot r \right) \cdot f_{c,IJ}(r), & r \le r_{s,1,IJ} \\ B_{IJ} \cdot \exp\left(-\lambda_{2,IJ} \cdot r \right) \cdot f_{c,IJ}(r) + A_{IJ} \cdot \exp\left(-\lambda_{1,IJ} \cdot r \right) \cdot f_{c,IJ}(r) \cdot \left[1 - f_{c,1,IJ}(r) \right], & r_{s,1,IJ} < r < r_{c,1,IJ} \\ B_{IJ} \cdot \exp\left(-\lambda_{2,IJ} \cdot r \right) \cdot f_{c,IJ}(r) + A_{IJ} \cdot \exp\left(-\lambda_{1,IJ} \cdot r \right) \cdot f_{c,IJ}(r), & r \ge r_{c,1,IJ} \end{cases} \\ F_{IJ}(X) = \left[1 + (\beta_{IJ} \cdot X)^{n_{IJ}} \right]^{-\frac{1}{2n_{IJ}}} \\ P_{IK}(\Delta r) = \exp\left[\lambda_{3,IK} \cdot \Delta r^3 \right] \\ W_{IK}(r) = f_{c,IK}(r) \\ G_{JIK}(\theta) = 1 + \dfrac{c_{IK}^2}{d_{IK}^2} - \dfrac{c_{IK}^2}{d_{IK}^2 + (h_{IK} + \cos\theta)^2} \end{cases}$$

(13)

where $f_{c,1,IJ}(r)$ is a cutoff function similar to equation (12) but operates at a different cutoff range:

$$f_{c,1,IJ}(r)=\begin{cases}1, & r \le r_{s,1,IJ} \\ \frac{1}{2}+\frac{1}{2}\cos\left[\frac{\pi(r-r_{s,1,IJ})}{r_{c,1,IJ}-r_{s,1,IJ}}\right], & r_{s,1,IJ} < r < r_{c,1,IJ} \\ 0, & r \ge r_{c,1,IJ}\end{cases} \tag{14}$$

and A_{IJ}, B_{IJ}, $\lambda_{1,IJ}$, $\lambda_{2,IJ}$, $\lambda_{3,IJ}$, β_{IJ}, n_{IJ}, c_{IJ}, d_{IJ}, h_{IJ}, $r_{s,1,IJ}$, and $r_{c,1,IJ}$ are all pairwise parameters. To use the polymorphic model for the embedded-atom method potential [22], we can simply set:

$$\begin{cases}\eta_{ij}=1-\delta_{ij}, \xi_{IJ}=0 \\ U_{IJ}(r)=\phi_{IJ}(r) \\ V_{IJ}(r)=1 \\ F_{II}(X)=-2F_{I}(X) \\ P_{IK}(\Delta r)=1 \\ W_{IK}(r)=f_{K}(r) \\ G_{JIK}(\theta)=1\end{cases} \tag{15}$$

where $\phi_{IJ}(r)$ is a pair function, $f_J(r)$ is an atomic electron density function, $F_I(X)$ is the embedding energy function, and X is used to represent electron density ($X = \rho$). We have implemented this polymorphic potential model in the public parallel MD codes LAMMPS [23].

4. PARAMETERIZATION

To enable ionic conduction of TlBr under external electric fields, it is mandatory to pursue a highly robust interatomic potential that at least maintain the equilibrium crystal structure of TlBr when Tl^+ and Br^- are subject to large opposite external forces due to a high electric field. To achieve this, we ensure that (1) the potential best reflect the experimental properties of the observed Tl, Br, and TlBr phases (e.g., Tl-hcp, TlBr-CsCl, etc.); and (2) the potential predicts the crystalline growth of the ground state structures during molecular dynamics simulations of

growth (e.g., vapor deposition). The growth simulation tests are important because they sample a variety of configurations (at the growth surface) not known a prior. If any of the random nuclei formed on the growth surface has a lower energy than the growth crystal, the simulations is likely to give an amorphous growth. Hence, crystalline growth provides strong validation that the growth crystal has the lowest energy compared with any other configurations. On the other hand, if TlBr can grow into to the correct CsCl type of equilibrium crystal during the growth simulations, it is likely that the CsCl type of crystal can be maintained when a large external electric field is applied to a TlBr bulk. Hence, the growth simulation capability is essential for our applications albeit it is difficult to achieve.

We proceed by parameterizing first the Tl and Br potentials, and then the TlBr potential at the known Tl and Br parameters. The observed room-temperature equilibrium phases are hcp for Tl [25], diatomic (Br_2) liquid for Br, and CsCl for TlBr [25]. Like many other potentials, our MSW model is not intended to capture the Br_2 molecules (it is possible to capture the Br_2 molecules, but this does not necessarily result in a better potential not to mention that the chemical reaction of elements is not relevant for studying TlBr bulk). However, our calculations with the density function theory indicated that the sc Br phase has a lower cohesive energy than dc, bcc, fcc, and hcp phases. Hence, we target sc as the lowest energy lattice phase for Br (at 0 K) while at the same time ensure that the stable Br phase at room temperature is liquid. Lattice constants, cohesive energies, and elastic constants for the lowest energy lattices (Tl-hcp, Br-sc, and TlBr-CsCl) are fitted under the constraints that the energies of all the other phases (e.g., dc, bcc, fcc, NaCl, wz, etc.) are higher than the targeted lowest energy phases. For the experimentally observed structures such as Tl-hcp and TlBr-CsCl, the experimental lattice constants [25], cohesive energies [26], and elastic constants [27,28] are directly used as the target

values for the fitting. For the phases that are not observed (e.g., Br-sc), the DFT results are used as the target values. DFT results may be quite different from the experimental values. For example, the hcp Tl cohesive energy obtained from experiments and DFT calculations is -1.85 and -2.40 eV/atom respectively. As a result, we scale the DFT results so that for the observed structures, the scaled DFT results match the experiments.

Mathematica [29] is used to perform the parameterization. To promote global optimization, four different numerical optimization routines, namely a conjugate gradient method [30], the downhill simplex method of Nelder and Mead [31], a genetic algorithm [32], and a biased random walk (simulated annealing) [33], are all used to determine the parameters that minimize the weighted mean-square deviation between the target and predicted properties. The goal to capture the crystalline growth is much more challenging, requiring a highly iterative parameterization process. After each fitting iteration, the four sets of parameters from the four optimization routines are tested for vapor deposition simulations. If an amorphous growth is detected, the entire process is repeated with an appropriate adjustment of parameters bounds, target structures and target properties. The iterations continue until one of the four optimization routines results in a satisfactory set of potential parameters. The MSW potential thus determined are listed in Tables (I) and (II) for two-body, and three-body parameters respectively.

Table I. Two-body parameters of MSW potential (length in Å and energy in eV)

IJ	$r_{0,IJ}$	$r_{s,IJ}$	$r_{c,IJ}$	$E_{b,IJ}$	$\alpha_{,IJ}$	$\beta_{,IJ}$	$\gamma_{,IJ}$
TlTl	3.02409	3.97219	4.26900	-0.514663	5.60012	3.39397	1.94224
BrBr	2.83451	3.60000	4.05800	-0.336014	7.00000	4.37500	3.00000
TlBr	2.98521	3.90480	4.73600	-0.747107	6.20000	2.00000	2.20000

Table II. Three-body parameters of MSW potential (length in Å and energy in eV)

IJK	TlTlTl	BrBrBr	TlTlBr (=BrTlTl)	TlBrBr (=BrBrTl)	TlBrTl	BrTlBr
λ_{JIK}	0.05000	0.13144	0.11804	0.05733	2.38107	2.38107
$\cos\theta_{0,JIK}$	0.07257	-0.50000	-0.53735	-0.54059	-0.29333	-0.29333

$\cos\theta_{1,JIK}$	-1.00000	-1.00000	-1.00000	-1.00000	-1.00000	-1.00000
$\cos\theta_{2,JIK}$	0.60000	0.60000	0.53947	0.56717	0.29333	0.29333
$\xi_{0,JIK}$	3.50000	0.62340	1.44291	2.79355	0.25182	0.25182
$\xi_{1,JIK}$	0.18625	2.60000	0.70848	1.42550	0.24026	0.24026
$\xi_{2,JIK}$	0.00000	0.00000	1.72178	2.04092	0.46849	0.46849
$\kappa_{1,JIK}$	0.20957	0.96000	1.00000	0.75390	1.00000	1.00000
$\kappa_{2,JIK}$	0.00000	0.00000	0.00000	0.27602	0.94796	0.94796

5. EVALUATION OF THE POTENTIAL

5.1 Lattice Constants and Cohesive Energies of Various Phases

Using the polymorphic potential model, calculations are performed to evaluate our TlBr potential. First, lattice constants and cohesive energies of various Tl, Br, and TlBr lattices are calculated using molecular statics energy minimization simulations. The results are summarized in Table III along with the available experimental data and our DFT values.

Table III. Lattice constants a and c (Å), and cohesive energy E_c (eV/atom), obtained from the MSW potential, DFT calculations, and experiments for selected material structures.

material	structure	MSW			DFT			Exp.		
		a	c	E_c	a	c	E_c	a [25]	c [25]	E_c [26]
Tl	dc	7.180	-----	-0.999	-----	-----	-----	-----	-----	-----
	sc	3.012	-----	-1.800	-----	-----	-----	-----	-----	-----
	bcc	3.854	-----	-1.805	3.868	-----	-2.368	-----	-----	-----
	fcc	4.825	-----	-1.848	4.873	-----	-2.340	-----	-----	-----
	hcp	3.408	5.582	-1.850	3.500	5.581	-2.399	3.450	5.520	-1.850
Br	dc	6.591	-----	-0.731	6.898	-----	-0.961	-----	-----	-----
	fcc	4.878	-----	-0.748	4.464	-----	-1.123	-----	-----	-----
	bcc	3.847	-----	-0.780	3.703	-----	-1.160	-----	-----	-----
	hcp	3.328	5.743	-0.787	-----	-----	-----	-----	-----	-----
	sc	3.004	-----	-0.827	3.006	-----	-1.218	-----	-----	-1.134*
TlBr	wz	4.877	7.964	-1.657	-----	-----	-----	-----	-----	-----
	zb	6.897	-----	-1.657	-----	-----	-----	-----	-----	-----
	NaCl	6.197	-----	-2.239	6.622	-----	-2.866	-----	-----	-----
	CsCl	3.985	-----	-2.389	3.959	-----	-2.881	3.985	-----	-2.389

*: Br-sc is the lowest energy lattice in models. No experimental data is available for the metastable Br-sc phase. Instead, we list the experimental cohesive energy of the lowest energy phase (Br_2-liquid) as a reference.

Table III indicates that of the lattice structures explored, our MSW potential captures the Tl-hcp, Br-sc, and TlBr-CsCl lattice crystals as the lowest energy phases. This agrees well with experiments or DFT in that Tl-hcp and TlBr-CsCl phases are observed experimentally at room temperature whereas Br-sc is predicted by DFT to have the lowest energy of all the lattice structures shown in Table III. Here we cannot include the Br_2 liquid observed in experiments in Table III. Instead, we will show below through growth simulations that our potential gives Br liquid as the most stable phase at room temperature. Here we can see that in addition to capturing the correct lowest energy phases, our MSW model also reproduces the experimental cohesive energies of Tl-hcp and TlBr-CsCl. Our energy of -0.827 eV/atom for Br-sc is not unreasonable compared with the experimental cohesive energy of -1.134 eV/atom for a more stable Br_2-liquid, especially considering that even DFT cannot accurately capture the absolute values of energies in the TlBr system. Note that MSW model also captures well the experimental lattice constant of TlBr-CsCl and DFT lattice constant of Br-sc. The lattice constants of Tl-hcp as prescribed by our MSW is not far off from the experimental values either because while the lattice constant a is slightly under-estimated, the lattice constant c is slightly over-estimated resulting in a better description of atomic volume.

Capturing non-tetrahedral crystals (such as hcp, sc, CsCl) as the lowest energy phases proves that the MSW potential has improved over the conventional SW potentials. SW potentials are not designed for capturing property trends of a variety of metastable structures. The purpose of listing some selected metastable phases in Table III is to show that the equilibrium phases have lower energies than these metastable phases. Interestingly, however, our MSW potential reproduces the DFT order of Br structures with increasing (more negative) cohesive energies as in dc $\rightarrow$ fcc $\rightarrow$ bcc $\rightarrow$ sc, suggesting that by capturing the correct low energy sc phase, the

transferability to a variety of other configurations can also be achieved. Usually such transferability is only possible with more sophisticated potentials. Since our MSW is designed for studying the TlBr bulk, the property trends of many metastable phases are not relevant and so we do not exploit this further for the Tl and TlBr phases which would necessarily sacrifice the properties of the equilibrium phases.

Finally, we point out that Table III only explores limited number of phases and therefore does not prove that the predicted lowest energy phases indeed have the lowest energies as compared to any other configurations. As will be discussed below, we will prove this rigorously through vapor deposition simulations.

5.2 Elastic Constants and Melting Temperature of the Observed Tl and TlBr Phases

Elastic constants and melting temperature of the experimentally observed Tl-hcp and TlBr-CsCl phases are calculated, and the results are summarized in Table IV along with the experimental values. Here the melting temperature calculations follow the same method described previously [34]. It can be seen that our MSW model reproduces the experimental elastic constants for TlBr-CsCl. The model elastic constants for Tl-hcp are generally lower than the experimental values. Note that we could have fit exactly the experimental elastic constants for Tl-hcp. However, this would result in a melting temperature that is significantly above the experimental value. The ability to prescribe the observed low elastic constants for closely packed elements is significant for the MSW model because the conventional SW potentials significantly overestimate these elastic constants.

Table IV. Elastic constants C_{11}, C_{12}, C_{13}, C_{33}, C_{44}, bulk modulus B (eV/Å^3), and melting temperature T_m (K) of the observed Tl and TlBr crystalline phases, obtained from the MSW potential and experiments.

structure	method	C_{11}	C_{12}	C_{13}	C_{33}	C_{44}	B	T_m
Tl (hcp)	MSW	0.240	0.140	0.137	0.242	0.053	0.133	691
	Exp. [27,35]	0.277	0.235	0.187	0.376	0.055	0.239	577

TlBr (CsCl)	MSW	0.275	0.104	0.104	0.275	0.067	0.161	1442
	Exp. [28,36]	0.275	0.104	0.104	0.275	0.067	0.161	753

We get the melting temperature of Tl-hcp reasonably close to the experimental value. Despite a prolonged effort, our current parameterization of the MSW potential still significantly overestimates the melting temperature of TlBr-CsCl. This may not be critical when studying structure evolution of TlBr-CsCl solids. Nonetheless, we point out that (1) due to small time and length scales, MD simulations are almost never performed under realistic conditions. Hence, MD simulations are effective to discover new phenomena, but the simulated results should be used to mainly elucidate the trends observed in experiments; and (2) the overestimated melting temperature should be kept in mind when interpreting the results especially if the system involves TlBr melt. Dependence of material properties on temperature relative to the melting point should be expressed in terms of homologous temperature.

D. Point Defects

Native point defects in TlBr-CsCl, including Tl vacancy V_{Tl}, Br vacancy V_{Br}, Tl at Br antisite Tl_{Br}, Br at Tl antisite Br_{Tl}, Tl interstitial between Tl sites $Tl_{i,1}$, Tl interstitial between Br sites $Tl_{i,2}$, Br interstitial between Tl sites $Br_{i,1}$, and Br interstitial between Br sites $Br_{i,2}$, are all studied. In particular, intrinsic defect energies $E_D^{'}$ are calculated as [37,38]

$$E_D^{'} = E - (N_{Tl} + N_{Br}) \cdot E_{TlBr} - 0.5 \cdot (N_{Tl} - N_{Br}) \cdot (E_{Tl} - E_{Br}) \quad (16)$$

where E, N_{Tl}, and N_{Br} are total energy, number of Tl atoms, and number of Br atoms of the system containing the defect, and E_{TlBr}, E_{Tl}, and E_{Br} are cohesive energies (per atom unit) for the lowest energy phases of TlBr, Tl, and Br respectively. The results obtained from MSW and DFT calculations are summarized in Table V. It can be seen that MSW potential a lower energy for Tl vacancy than for Br vacancy, a low energy for Br at Tl antisite than for Tl at Br

antisite, lower energies for Br interstitials than for Tl interstitials. All these are in good agreement with the DFT calculations. Again here we can only compare the trends, and cannot make conclusions on the absolute values due to the lack of experimental data.

Table V. Intrinsic defect energy $E_D^{'}$ (eV) obtained from different models for TlBr-CsCl.

method	V_{Tl}	V_{Br}	Tl_{Br}	Br_{Tl}	$Tl_{i,1}$	$Tl_{i,2}$	$Br_{i,1}$	$Br_{i,2}$
MSW	1.04	1.29	2.75	1.05	2.93	3.03	2.00	2.00
DFT	0.63	1.59	3.53	1.66	2.19	2.58	2.29	1.56

6. MOLECULAR DYNAMICS VAPOR DEPOSITION VERIFICATIONS

As mentioned above, only when a potential captures the crystalline growth during MD vapor deposition simulations will it be robust enough to study the ionic conduction under a high electric field. In addition, crystalline growth simulation capability is a rigorous proof that the potential captures the lowest energy phases, albeit such a capability is extremely difficult to achieve. Here we perform vapor deposition simulations to validate that our TlBr MSW potential captures the crystalline growth of the lowest energy Tl-hcp and TlBr-CsCl crystals. In addition, we will demonstrate that our potential captures the crystalline growth of Br-sc at a low temperature but gives a liquid Br structure as the stable phase at room temperature.

6.1 Tl-hcp Growth

For Tl-hcp growth, an initial substrate of an hcp crystal containing 1008 Tl atoms with 28 $(2\bar{1}\bar{1}0)$ layers in the x direction, 9 (0002) layers in the y direction, and 8 $(0\bar{1}10)$ layers in the z direction is used. Here layers refer to crystallographic planes so that one (0001) layer is equivalent n (000n) layers etc. The substrate temperature is set at T = 300 K by assigning velocities to atoms according to the Boltzmann distribution. During simulations, the bottom (-y) 2 (0002) layers are held fixed to prevent crystal shift upon adatom impact on the top surface. The

next 3 (0002) layers are isothermally controlled at the substrate temperature. This leaves the top 4 layers free where the motion of atoms is solely determined by Newton's law. Injection of Tl adatoms from random locations far above the surface simulates the growth. All adatoms have an initial far-field incident kinetic energy $E_i = 0.05$ eV and an incident angle $\theta = 0^o$ (i.e., the moving direction is perpendicular to the surface). The adatom injection frequency is chosen to give a deposition rate of R = 2.5 nm/ns. To approximately maintain a constant thickness of the free surface region, the isothermal region expands upward during simulations. Since surface roughness might develop, the isothermal region expands at about 80% of the surface growth rate to ensure that the upper boundary of the isothermal region never exceeds the surface valley locations. Fig. 1 shows the resulting configuration obtained after 0.66 ns deposition, where the original substrate is shaded in purple. It can be seen that the MSW potential correctly captures the crystalline growth of the Tl-hcp phase. This strongly validates that Tl-hcp has the lowest energy at room temperature as compared to any other configurations.

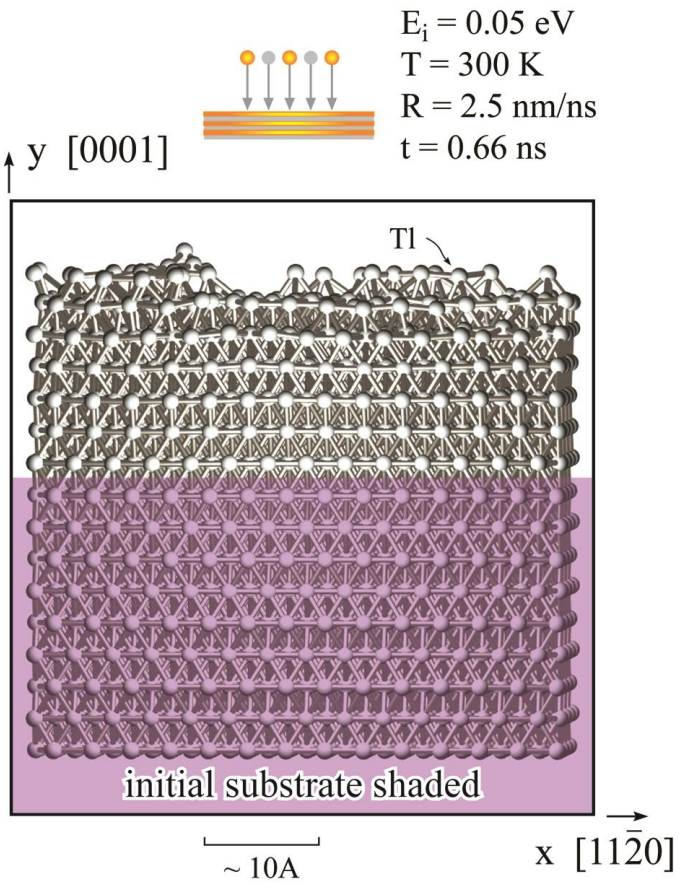

Fig. 1. Vapor deposited hcp Tl film obtained from MD simulations.

6.2 Br-sc Growth

MD simulations are also performed to grow Br on an Br-sc substrate. A sc crystal containing 1008 Br atoms with 14 (100) layers in the x direction, 9 (010) layers in the y direction, and 8 (001) layers in the z direction is used as the initial substrate. During simulations, the bottom 2 (020) layers are held fixed. The next 4 (020) layers are controlled at the desired growth temperature. Using the same approach as described above, the growth simulation is performed at two substrate temperatures T = 150 K and T = 300 K, an incident energy E_i = 0.05 eV, an incident angle $\theta = 0^o$, and a deposition rate R = 2.5 nm/ns. The resulting configurations obtained after 1.20 ns deposition are shown in Figs. 2(a) and 2(b) respectively for the 150 K and 300 K temperatures. It can be seen from Fig. 2(a) that the crystalline growth of the sc crystal is

achieved with our potential, strongly validating that the Br-sc structure have the lowest (free) energy at 150 K as compared with any other configurations. Fig. 2(b), on the other hand, indicates an amorphous growth at 300 K. This strongly validates that Br exhibits a liquid phase at room temperature.

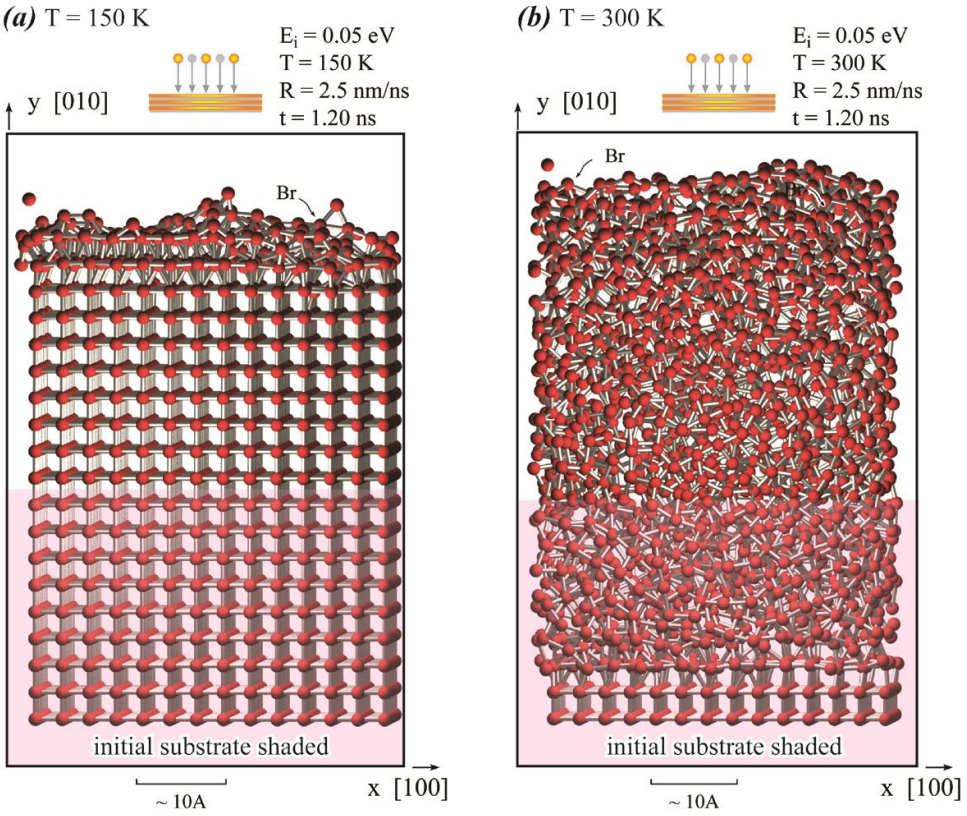

Fig. 2. MD simulations of Br growth on a Br-sc substrate at a temperature of (a) 150 K and (b) 300 K. Our potential prescribes a liquid Br as the most stable phase at room temperature.

6.3 TlBr-CsCl Growth

For TlBr-CsCl growth, an initial TlBr substrate of a CsCl type of crystal containing 300 Tl atoms and 300 Br atoms with 20 (200) layers in the x direction, 10 (020) layers in the y direction, and 12 (002) layers in the z direction is used. Initially, Br terminates the top y surface. During simulations, the bottom 3 (020) layers are held fixed. The next 4 (020) layers are controlled at the desired growth temperature. Following the same approach as described above,

the growth simulation is performed at a substrate temperature T = 700 K, an incident energy E_i = 0.05 eV, an incident angle $\theta = 0^o$, a deposition rate R = 2.75 nm/ns, and a stoichiometric vapor flux ratio Tl:Br = 1:1. Fig. 3 shows the system configuration obtained at 0.78 ns deposition time. It is seen again that our MSW potential correctly captures the crystalline growth of the equilibrium (CsCl) phase of TlBr. In particular, the randomly injected Tl and Br atoms are reconstructed correctly to their corresponding sublattices. Because the potential captures the crystallization from a rather stochastic vapor phase, it enables robust simulations of ionic conduction by maintaining the CsCl crystal under conditions where the presence of dislocations and external electric fields may both induce configuration disorders.

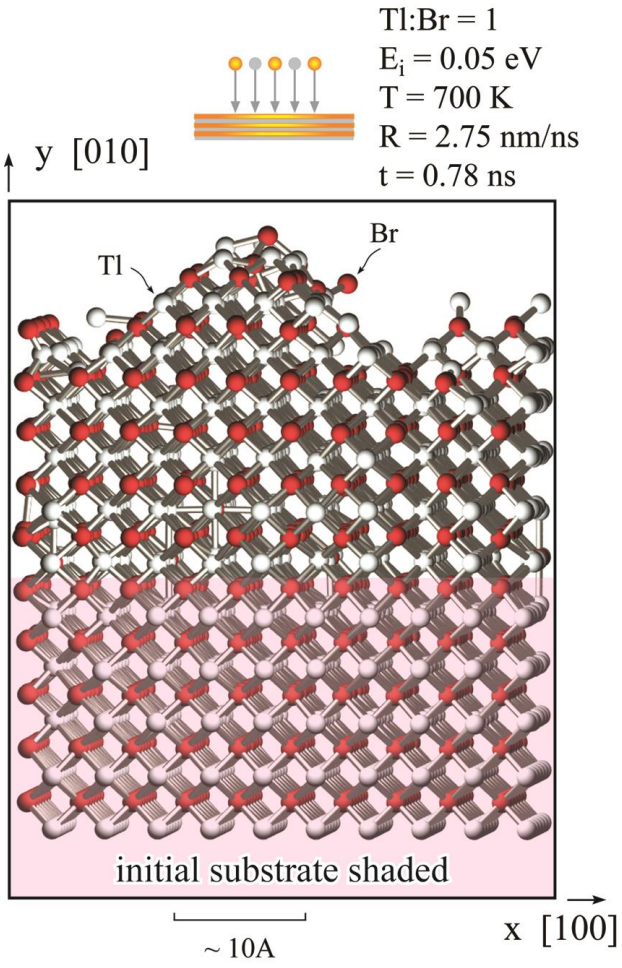

Fig. 3. Vapor deposited CsCl phase of a TlBr film obtained from MD simulations.

7. MOLECULAR DYNAMICS IONIC CONDUCTION

One major objective of the present work is to allow direct MD simulations of ionic conduction of TlBr-CsCl crystal under a very high external electric field. The external electric field can be simulated by applying opposite biased forces to Tl and Br atoms. The simulations become challenging at large external forces (i.e., electric fields) as these forces may destroy the stability of the CsCl crystal. Here we demonstrate two cases to demonstrate that our potential allows simulations to be performed when atoms are subject to large forces of ±0.4 eV/Å. Note that these forces correspond to a high electric field of 4×10^6 V/mm assuming Tl and Br atoms adopt full charges of ±1 e. Since charges on Tl and Br atoms are significantly smaller in real crystals, the external field should be much larger than 4×10^6 V/mm.

A TlBr-CsCl crystal containing 16128 Tl atoms and 16128 Br atoms with 84 (110) layers in the x direction, 24 $(\bar{1}10)$ layers in the y direction, and 32 (002) layers in the z direction is used. To prevent system from shifting, the bottom region of about 10 Å wide is fixed. To remove the boundary effects, periodic boundary conditions are used in all three coordinate directions. MD simulation is then performed at a temperature of 1200 K temperature (a homologous temperature 0.832 T_m) and a biased force of ±0.4 eV/Å using the NVT ensemble (i.e., number of atoms, volume, and temperature are all constant).

In the first case, we assume that the system contains a pair of Tl and Br vacancies by removing one Tl and one Br atoms that are far away from the fixed region. Comparison of atomic configurations between a time span of 0.06 ns is shown in Fig. 4. Fig. 4 verifies that our potential indeed allows stable TlBr-CsCl MD simulations at a very high biased force. Interestingly, we found that Tl and Br vacancies are not very mobile even at the high biased

force and the high temperature. In fact, during the 0.06 ns span, Tl vacancy jumped by one lattice spacing whereas the Br vacancy did not jump.

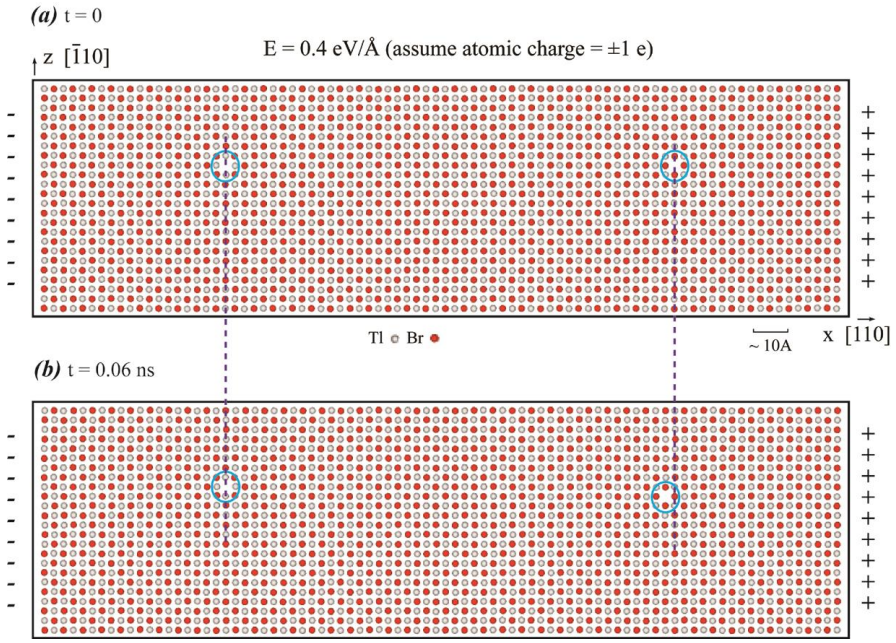

Fig. 4. Vacancy ionic conduction simulation at a temperature of 0.832 T_m and a biased force of ±0.4 eV/Å: (a) Starting time of observation; and (b) 0.06 ns later. The TlBr-CsCl crystal remains intact at the large electric field. During the 0.06 ns span, Tl vacancy jumped by one lattice spacing whereas the Br vacancy did not jump.

In the second case, we assume that the system contains a pair of Tl and Br interstitials by inserting one Tl and one Br atoms that are far away from the fixed region. Comparison of atomic configurations between a time span of 0.12 ns is shown in Fig. 5. Fig. 5 again verifies that our potential allows stable TlBr-CsCl MD simulations at a very high biased force. Unlike the vacancy case, we found that Tl and Br interstitials are very mobile, and both interstitials moved a significant distance during the 0.12 ns time span.

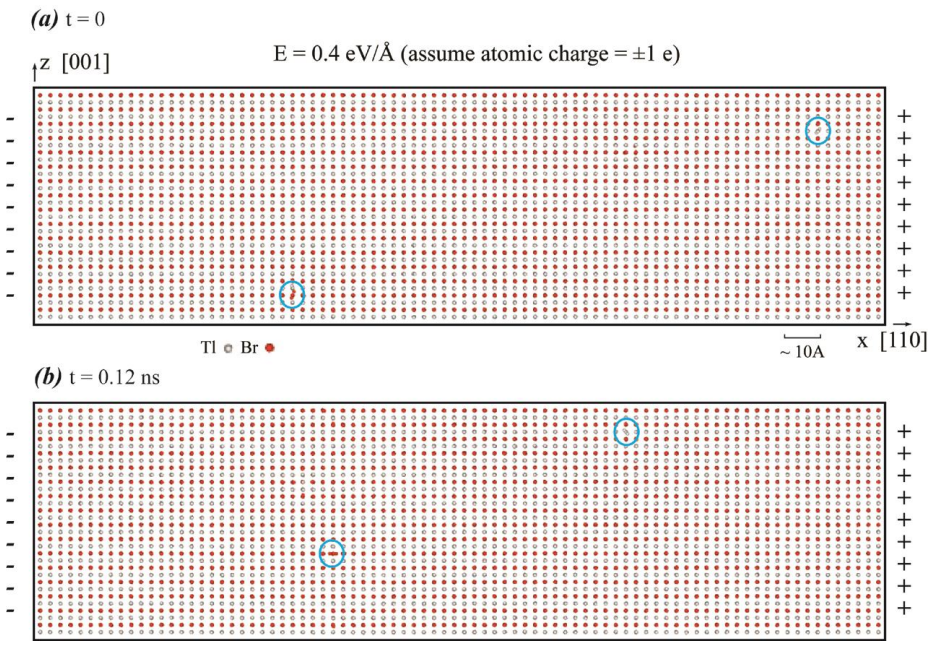

Fig. 5. Interstitial ionic conduction simulation at a temperature of 0.832 T_m and a biased force of ±0.4 eV/Å: (a) Starting time of observation; and (b) 0.12 ns later. The TlBr-CsCl crystal remains intact at the large electric field. During the 0.12 ns span, Tl and Br interstitials migrated significant distances.

8. CONCLUSIONS

This work has developed a new modified Stillinger-Weber potential. Unlike the conventional SW potential that significantly overestimates the elastic constants of closely packed elements and are limited mainly to tetrahedral structures, our modified potential can capture very low elastic constants for closely packed elements and can be used for many non-tetrahedral crystal structures. We have parameterized the modified SW potential for TlBr. Through rigorous vapor deposition simulation tests, we have demonstrated that this TlBr captures well the experimental properties of the observed Tl and TlBr phases, and give the Br liquid as the most stable phase at room temperature. Most importantly, we have demonstrated our potential allows challenging simulations of ionic conduction of TlBr crystals under very high external electric fields. Test simulations already indicate that interstitials migrate much faster than vacancies. We

have also developed a polymorphic potential model and implemented it in public MD codes LAMMPS. This essentially enables future material research to be performed at a higher fidelity level because improved potentials no longer require modification of the MD codes and therefore can immediately applied by a broader materials and physics community.

9. ACKNOWLEDGEMENTS

Sandia National Laboratories is a multiprogram laboratory managed and operated by Sandia Corporation, a wholly owned subsidiary of Lockheed Martin Corporation, for the US Department of Energy's National Nuclear Security Administration under contract DE-AC04-94AL85000. This work was performed under a Laboratory Directed Research and Development (LDRD) project.

1 M. Shorohov, M. Kouznetsov, I. Lisitskiy, V. Ivanov, V. Gostilo, and A. Owens, IEEE Trans. Nucl. Sci., 56, 1875 (2009).
2 K. Hitomi, M. Matsumoto, O. Muroi, T. Shoji, and Y. Hiratate, IEEE Trans. Nucl. Sci., 49, 2526 (2002).
3 K. Hitomi, Y. Kikuchi, T. Shoji, and K. Ishii, IEEE Trans. Nucl. Sci., 56, 1859 (2009).
4 J. X. M. Zheng-Johansson, and R. L. McGreevy, Solid State Ionics, 83, 35 (1996).
5 J. X. M. Zheng-Johansson, I. Ebbsjo, and R. L. McGreevy, Solid State Ionics, 82, 115 (1995).
6 C. W. Huang, W. C. J. Wei, C. S. Chen, and J. C. Chen, J. Euro. Cer. Soc., 31, 3159 (2011).
7 K.-L. Tung, K.-S. Chang, C.-C. Hsiung, Y.-C. Chiang, and Y.-L. Li, Separation Purification Tech., 73, 13 (2010).
8 D. Marrocchelli, P. A. Madden, S. T. Norberg, and S. Hull, Chem. Mater., 23, 1365 (2011).
9 Y. Yamamura, S. Kawasaki, and H. Sakai, Solid State Ionics, 126, 181 (1999).
10 R. W. J. M. Huang Foen Chung, and S. W. de Leeuw, Solid State Ionics, 175, 851 (2004).
11 J. V. L. Beckers, K. J. van der Bent, and S. W. de Leeuw, Solid State Ionics, 133, 217 (2000).
12 P. J. D. Lindan, and M. J. Gillan, J. Phys.: Condens. Matter, 5, 1019 (1993).
13 F. H. Stillinger and T. A. Weber, Phys. Rev. B 31, 5262 (1985).
14 X. W. Zhou, D. K. Ward, J. E. Martin, F. B. van Swol, J. L. Cruz-Campa, and D. Zubia, Phys. Rev. B, 88, 085309 (2013).
15 X. W. Zhou, R. E. Jones, C. J. Kimmer, J. C. Duda, and P. E. Hopkins, Phys. Rev. B, 87, 094303 (2013).
16 X. W. Zhou, R. E. Jones, J. C. Duda, and P. E. Hopkins, Phys. Chem. Chem. Phys., 15, 11078 (2013).
17 X. W. Zhou, M. E. Foster, J. E. Martin, and F. B. van Swol, Phys. Rev. B, ??.

18 J. Wang, and A. Rockett, Phys. Rev. B 43, 12571 (1991).
19 J. Tersoff, Phys. Rev. B 39, 5566 (1989).
20 K. Albe, K. Nordlund, J. Nord, and A. Kuronen, Phys. Rev. B 66, 035205 (2002).
21 X. W. Zhou, and R. E. Jones, Modelling Simul. Mater. Sci. Eng., 19, 025004 (2011).
22 M. S. Daw, and M. I. Baskes, Phys. Rev. B, 29, 6443 (1984).
23 S. Plimpton, J. Comput. Phys., 117, 1 (1995). lammps.sandia.gov.
24 D. G. Pettifor, M. W. Finnis, D. Nguyen-Manh, D. A. Murdick, X. W. Zhou, and H. N. G. Wadley, Mater. Sci. Eng. A, 365, 2 (2004).
25 J. D. H. Donnay, and H. M. Ondik, "crystal data, determinative tables", 3rd ed., Vol. 2 (inorganic compounds), U. S. Department of Commerce, National Bureau of Standards, and Joint Committee on Power Diffraction Standards, U. S. A., 1973.
26 I. Barin, "thermochemical data of pure substances", VCH, Weinheim, 1993.
27 G. Simmons, "single crystal elastic constants and calculated aggregate properties", Southern Methodist University Press, 1965.
28 G. E. Morse, and A. W. Lawson, J. Phys. Chem. Solids, 28, 939 (1967).
29 S. Wolfram, The Mathematica Book, 5th ed. (Wolfram Research, Inc., Champaign, IL, 2004), p. 106ff.
30 M. R. Hestenes, and E. Stiefel, J. Res. National Bureau Stand., 49, 409 (1952).
31 D. M. Olsson, and L. S. Nelson, Technometrics, 17, 45 (1975).
32 R. Storn, and K. Price, J. Global Opt., 11, 341 (1997).
33 S. Kirkpatrick, C. D. Gelatt, and M. P. Vecchi, Science, 220, 671 (1983).
34 X. W. Zhou, M. E. Foster, F. B. van Swol, J. E. Martin, and B. M. Wong, J. Phys. Chem. C, 118, 20661 (2014).
35 Y. P. Afinogenov, and T. N. Larionova, Russ. J. Inorg. Chem., 37, 1344 (1992).
36 H. Kim, A. Churilov, G. Ciampi, L. Cirignano, W. Higgins, S. Kim, P. O'Dougherty, F. Olschner, and Kanai Shah, Nucl. Ins. Meth. Phys. Res. A, 629, 192 (2011).
37 S. B. Zhang, and J. E. Northrup, Phys. Rev. Lett., 67, 2339 (1991).
38 J. E. Northrup, and S. B. Zhang, Phys. Rev. B, 47, 6791 (1993).